i-ETC: ISEL Academic Journal of Electronics, Telecommunications and Computers
IoT-2018 Issue, Vol. 4, n. 1 (2018) ID-5

Passive Optical Communications Module for the Internet of Things

Ribeiro,T.[a]

[a] Department of Electrical and Computer Engineering, Instituto Superior Técnico

tiagorib93@gmail.com

Abstract **- The Internet of Things (IoT) promotes interconnectivity between devices and these keep appearing in larger quantities throughout the years, with the evolution of communication technologies. However, scalability comes with a price, since for a higher quantity of devices comes the need for better transmission channels, with higher reach, availability and improved security capabilities.**

Wireless technologies already provide a way to solve these issues, but the use of optical fibers would give to the IoT their own unique features. But IoT devices should not be power hungry nor have costly electrical-to-optical conversions, so a passive optical communications module based of fiber Bragg should be implemented. This module would be integrated in the IoT ecosystem by connecting it to the many existent dark fibers all over the world.

A simulator of this module was implemented, capable of reproducing its characteristics for the transmission of information modulated in Frequency-Shift Keying and On-Off Keying modulation schemes.

Keywords: Internet of Things, Fiber Bragg Gratings, Acousto-Optic Modulator, Frequency-Shift Keying, On-Off Keying

I. Introduction

The increase in Internet traffic over these past decades was only made possible with the deployment of a worldwide optical network. The long-haul fiber networks have evolved into a complex web with mesh connectivity in metropolitan areas, pushing the fiber into the edge of the network, thus forming a Fiber-To-The-Home (FTTH) network. Therefore, the fiber is no longer used solely for intercity links, but also supports metro and last-mile connectivity. It can also be found in industrial plants, alongside highways, remote rural roads, power transmission lines and railways. Of course, with this large presence of optical fiber cables, there are some spare fibers available, known as dark fibers, that can be explored for broadband capability and for providing basic connectivity with newly developed technologies [1].

However, the human ability to consume information is no longer the only drive for setting the limits to the required network bandwidth, but the by now dominant amount of Machine-to-Machine (M2M) traffic that rises from data-centric applications, sensor networks and the growing penetration of the Internet of Things (IoT). The IoT can and will impact manufacturing and supply chains from industries around the world, whose main goal is to increase efficiency by controlling their machines remotely, where environmental conditions may be unfavorable to allow wireless networks to operate.

For a certain industry to achieve this objective, it must use fiber optic cables which, due to the previously mentioned characteristics, are the best medium for the handling of information that is transmitted throughout the facility. This, of course, will lead to a growth of in-building fiber deployments not only for industrial facilities, but also for residential buildings which cannot be reached wirelessly [2].

The IoT can be considered as a global network which provides communication between human-to-human, human-to-things and things-to-things, each one with their own unique identity. However this requires a global infrastructure of networked physical objects that enables anytime, anyplace connectivity for anything, not only for any one [3].

A. Motivation and main objectives

In 2016, at the 21st OptoElectronics and Communications Conference, it was stated that, by the year of 2019, 83% of global data traffic is expected to come from cloud services and applications and it will gather a total data of 10.4 zettabytes per year [4].

By the year of 2008, the total number of interconnected devices over the Internet exceeded the world's population for the first time, and the trend of attaching more "things" of daily use to this network is accelerating. It is estimated that by the year of 2020, the number of devices connected with each other over the Internet, the so called Internet of Things, is expected to be around 50 billion, as depicted in figure 1, with the left axis referring to the world's population and internet-connected devices and the right one, the internet-connected devices per person.

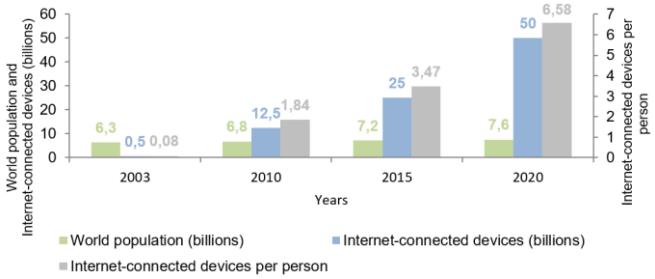

Fig. 1: Bar chart of the number of connected devices compared to the world's population [1].

The IoT limits are mainly based on the economic value that its featured services provide to society. The deployment of computational and storage capacities to support these services depends on the potential profits and gains obtained from building an infrastructure. If this network continues to be increasingly more ubiquitous, the investment in these infrastructures will still increase and the doubt remains if the same number of large companies will keep paying for it. Thus innovation needs to happen in a way in which the cost of new

components designed for optical fiber systems are reduced considerably [5].

For the IoT's transmission layer, the aim is to transfer data over long distances or large areas. Several wireless standards for IoT applications such as Zigbee and Wi-Fi are capable of successfully transmitting data to a given end-user, although, for an industrial application, a wired solution is more feasible. Wireless communications for wide areas have several issues such as spectrum usage, causing loss of the quality of the signal, and the environment topography, from which comes the degradation of the transmitted signals due to the distance getting bigger and because of the multipath fading effects that may also induce signal-to-noise fluctuations that may cause unreliability towards the requirements for providing connectivity for critical IoT applications. Adding to these issues, the broadcasting nature of wireless connectivity has some evidently fundamental privacy and security vulnerabilities. An optical wired communication system can be adopted to contradict these issues, since the optical fiber offers a huge bandwidth with very low attenuation, typically 0.2 dB/km for a standard Single Mode Fiber (SMF), allowing the transmission of data over tens of kilometers.

The concept of IoT over Fiber (IoToF) uses Fiber Bragg Gratings (FBGs) to modulate the information coming from IoT devices in the optical carrier and transmit it over a large distance of over tens or maybe thousands of kilometers, when optical amplification schemes are used. The connection of this novel technology with the already existent optical fiber pipeline is done by using the dark fibers available, which are key for the IoT concept. To provide the direct physical connectivity (PHY) to IoT devices themselves might seem an overkill solution, but this would be viable and applicable when availability, reliability, security and other limiting factors handicap the physical connectivity solution already based on wireless and other wireless technologies. The IoToF system can be used in the monitorization of urban areas with a crowded and/or polluted spectrum, power lines structure and environment monitoring, collecting data in the gas and oil industries. Also, it can be used in wildfire monitoring in extremely remote locations, since the dense forests in hilly regions can create very unfavorable wireless propagation environments.

B. State of the art

Several wireless standards for IoT applications have been proposed during the last two decades, with table 1 depicting the comparison between the wireless IoT technologies and the novel IoToF introduced in this study.

Table I
WIRELESS IOT TECHNOLOGIES AND THE IOTOF CONCEPT

Technology	Data Throughput (bps)	Range (km)	Bandwidth (MHz)	Spectral Efficiency (bps/Hz)
LTE eMTC	1×10^6	11	1.4	0.714
Wi-Fi IEEE 802.11ac	500×10^6	0 1 via mesh	80	6.25
Bluetooth	2×10^6	0.75	2	1
Thread	250×10^3	0 1	5	0.05
Zigbee	250×10^3	0.13 LoS	2	0.125
Z-Wave	100×10^3	0.03	0.2	0.5
LoRa	22×10^3	30 (water) 15 (ground)	0.250	0.088
Sigfox	100	30	0.2	0.0005
IoToF	300	>30	0.0008	0.375

The continuous increase of traffic calls for the deployment of a worldwide optical network in which long-haul fiber networks form a complex web of mesh connectivity in metropolitan areas. Also, with Wavelength Division Multiplexing (WDM) techniques, these optical fibers can support several bandwidth-hungry applications [1].

Despite also enabling the IoT ecosystem over optical fibers, the IoToF concept presented in this study is a niche solution to fill the gaps from an IoT arena dominated by extremely low cost and widespread wireless solutions, therefore one of the main challenges in this novel developed system is the ease of capital and operational costs (CAPEX and OPEX, respectively). However, optical solutions are costly, not because of the optical fiber itself, but because they involve Electrical-to-Optical (E/O) and Optical-to-Electrical (O/E) interfaces. Such interfaces are usually power-hungry circuits, whereas optical fibers are electrically passive elements. Thus, energy presents itself as a major constraint for IoT solutions and these conversions need to be addressed in IoToF PHY architectures before benefiting from long-reach with reliability, privacy and other appealing features that optical fibers have, contrasting with the wireless ones.

Table 2 depicts some matching factors between conventional optical communication connectivity and the proposed IoToF PHY architecture. The data throughput required by individual IoT devices are usually several orders of magnitude below what the optical interfaces can offer. Long reach reliability from optical fibers is what IoToF aims to achieve in the IoT ecosystem, thus these requirements cannot be compromised by low cost optical solutions, i.e., based on LEDs, for example. Installation and maintenance in conventional optical systems is costly and time-consuming at E/O and O/E interfaces, since these involve specialized splicing equipment and connectors, whereas the wireless counterpart operation is virtually effortless and costless. With this in mind, IoToF should be aimed at extremely simple operations.

Table II
IOT REQUIREMENTS AND CONVENTIONAL OPTICAL AND IOTOF PHYS [6-8].

IoT Requirements	Conventional Optical PHY @ ONU (per subscriber)	IoToF Optical PHY
Throughput	Up to 2.5 Gbps	At least 100 bps
Range	Up to 20 km	At least 20 km
Power Consumption	around 1 W	0 W (Passive)

Also, conventional optical communication E/O and O/E conversions are power consuming due to the need of biasing and cooling circuitry, while IoToF would aim, if possible, at optical passive solutions at IoT devices. Spectral efficiency is not a major concern in optical systems seen in the widespread use of OOK and direct detection to reduce cost. In contrast, the extremely low-cost requirement from the IoT systems will push IoToF solutions with limited end-to-end bandwidth and, therefore, spectral efficiency will become an issue to be addressed [9].

Figure 2 depicts the comparison that can be made between the discussed technologies both in terms of bandwidth, which is related to the data throughput through the spectral efficiency, and the transmission distance. These parameters lead to a trade-

off correlated to the frequency bands, i.e., higher frequency bands have more channels and more bandwidth, which allows for more data throughput, however, the transmission range is much lower. On the opposite hand, lower frequency radio waves are less vulnerable to propagation disturbances than the higher ones, presenting a higher operation range, but the data throughput is reduced [10].

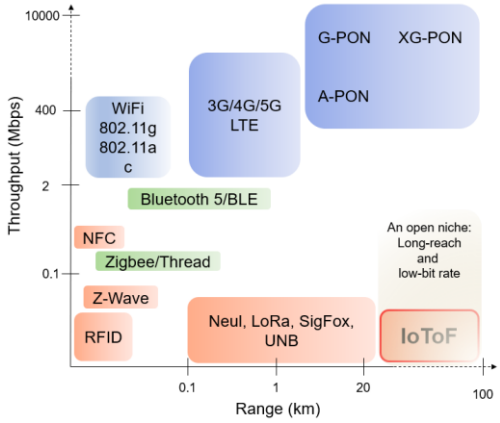

Fig. 2. Relation between throughput and range for IoT standards, with the inclusion of the novel IoToF concept.

In sum, IoToF should aim at ranges beyond conventional wireless solutions, but without compromising minimal throughputs achieved by them. This novel technology is therefore expected to exceed a fundamental wireless limit, i.e., the Radio Horizon Range (RHR), which is the furthest reach imposed by the earth's curvature Line-of-Sight (LoS) propagation, including the atmosphere's refraction effects. The RHR for a 30 m height gateway antenna and a base station at 1 m is around 20 km, which is proved experimentally as an achievable range by LoRa and Sigfox. This is also G-PON's basic reach, thus 20 km provides for an important optical and wireless landmark for IoToF to surpass and find its own niche [7, 11, 12].

II. Theoretical Foundation

A. Fiber Bragg Grating Technology

During the development of fiber optics technology, FBGs were applied in many photonic devices. An FBG is an optical filter inscribed in a short segment of an optical fiber, so that it can reflect specific wavelengths coming from a certain optical source and transmit all others. It can also be regarded as a fiber device with periodical variation of the refraction index of the core along the fiber [13].

Due to this successful implementation, FBGs proved their utility in a wide set of communication applications in the optical realm. They can be used as add/drop multiplexers for WDM resulting in an increased capacity of optical networks, as mode converters, as dispersion compensators and as pulse compressors [14].

Also, by studying the displacement of a given reference wavelength it is possible to measure several physical parameters, such as temperature, pressure, strain, etc. Thus, FBGs can be used as sensors and have many advantages, like the lack of LoS requirement, resistance to corrosion, immunity to electromagnetic interference and the easiness of implementation in miniaturization. Also very important, is the fact that it facilitates the remote control and processing of the information, simply because both sensing and propagation are rolled into one [4, 13, 15].

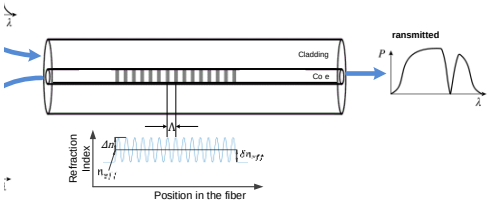

Fig.3. Schematic of the FBG with the spectral input and outputs.

From the first order Bragg condition results the reflected wavelength, also called the Bragg wavelength and it is given by the expression in equation 2.1:

$$\lambda_B = 2\Lambda n_{eff} \qquad (2.1)$$

where λ_B is the central Bragg wavelength of the reflected signal, n_{eff} is the effective refraction index of the optical fiber, which is an average of the refraction index of the core and of the cladding, and Λ is the period of the modulation of the refraction index in the core of the fiber.

The periodic perturbation of the refraction index (δn_{eff}) along the propagation axis z can be described by equation 2.2:

$$\delta n_{eff}(z) = \overline{\delta n_{eff}}(z)\left\{1 + \xi(z)\cos\left[\frac{2\pi}{\Lambda}z + \phi(z)\right]\right\} \qquad (2.2)$$

where $\overline{\delta n_{eff}}$ is the variation of the mean value of the modulation, ξ is the fringe visibility of the index change varying from 0 to 1, and $\phi(z)$ describes grating chirp for aperiodic gratings [16, 17].

For a periodic single-mode Bragg reflection grating the relations depicted in equations 2.3 and 2.4 are known:

$$\delta = 2\pi n_{eff}\left(\frac{1}{\lambda} - \frac{1}{\lambda_B}\right) \qquad (2.3)$$

$$\kappa = \frac{\delta n_{eff}\pi}{\lambda} \qquad (2.4)$$

From equation 2.3, comes the value called the detuning, which is independent of z for all gratings. To simplify the upcoming equation 2.6, it is useful to define the following variable of equation 2.5:

$$\gamma = \sqrt{\kappa^2 - \delta^2} \qquad (2.5)$$

Using the previous equations, the reflectivity of a grating with constant modulation amplitude and period is obtained as function of the wavelength λ and the length L of the grating, as shown in equation 2.6:

$$R_{\lambda,L} = \frac{\sinh^2(\gamma L)}{\cosh^2(\gamma L) - \frac{\delta^2}{\kappa^2}} \qquad (2.6)$$

B. FBG's manufacture techniques

There are many grating manufacture techniques, but in this study only the phase mask technique and the interferometer with phase mask technique will be considered.

The optical element known as the phase mask is made from

a flat slab of silica glass, which is transparent to UV light, and it features a periodic pattern shape that approximates a square wave in profile. The UV light, which is incident normally to the phase mask, passes through it and is diffracted by the periodic corrugations of the mask. These corrugations are almost in contact with the optical fiber. Usually, most of the diffracted light is contained in the 0, +1 and -1 diffracted orders, however, the phase mask is designed in such a way that it is able to suppress the diffraction into the zero-order to less than 5% and can divide 40% of the total light intensity equally in the $^{+}_{-}1$ orders, approximately. In other words, the zero-order diffraction is minimized and the +1 and -1 orders are maximized. The interference of these maximized order beams produce a periodic pattern that photoimprints a corresponding grating in the fiber.

The obtained period of the grating pattern in the core of the fiber is $\Lambda = \Lambda_{\mathrm{PM}}/2$, where Λ_{PM} is phase mask period [17, 18].

The phase mask technique can also be used to manufacture gratings with controlled spectral response characteristics. The typical spectral response of a finite length grating with a uniform index modulation along the fiber length has a secondary maximum on both sides of the main reflection peak. In WDM applications this kind of response is not desirable, so in order to avoid secondary maxima, a bell-like functional shape is given to the FBG. This process is called apodisation, which through the years have achieved suppressions of the sidelobes of 30 dB to 40 dB, using the phase mask technique [18].

The apodisation technique also extends to the manufacture of Chirped FBGs (CFBGs), also known as aperiodic fiber gratings, which are used for making dispersion compensators. The chirping aspect means varying the grating period along the length of the fiber in order to broaden its spectral response [18].

In the context of "Amplitude-splitting Interferometer" [17], the fringe grating period can me altered by varying the incidence angle, α, or by modifying the wavelength of the incident radiation, λ_{UV}. The choice of this wavelength is limited to the UV photosensitivity region of the fiber, however, there is no restriction for the choice of the angle α. The amplitude-splitting interferometer offers the ability to inscribe Bragg gratings of various characteristics, but it is susceptible to mechanical vibrations. This disadvantage originates from sub-micron displacements in the position of the mirrors, the beam splitter, or other optical mounts in the interferometer during UV irradiation, causing the fringe pattern to drift [19].

In the interferometer with phase mask technique, the UV beam splitting is done by a phase mask. The diffracted orders are reflected on lateral mirrors and are recombined in the fiber where they interfere with a certain pattern.

A phase mask, instead of an amplitude splitter, is used because, besides its economical factor, the alignment process is simplified. The wavelength of the designed grating is controlled by the incidence angle of the two diffracted orders on the fiber, which can be controlled by the lateral mirrors [17].

C. FBG's behavior due to external disturbances

The effective refraction index and the period modulation, both mentioned in equation (2.1), change with temperature and strain, thus changing the Bragg wavelength. The change in the reflected wavelength when exposed to variations in temperature, ΔT, and/or mechanical deformations, Δl, is given by equation 2.7 [13]:

$$\Delta\lambda_B = 2\left(\Lambda\frac{\partial n_{eff}}{\partial T} + n_{eff}\frac{\partial\Lambda}{\partial T}\right)\Delta T + 2\left(\Lambda\frac{\partial n_{eff}}{\partial l} + n_{eff}\frac{\partial\Lambda}{\partial l}\right)\Delta l \qquad (2.7)$$

An applied longitudinal deformation changes the Λ parameter due to the increasing pitch of grating and changes the n_{eff} parameter, because of the photoelastic effect. The latter comes from an observation made when compressing a transparent material, in which two effects can be observed, one is the increase of the refractive index due to the increase of density of the material and the other is the mentioned photoelastic effect, which produces the opposite effect.

In an equal manner, both parameters from the fundamental Bragg condition can be changed due to a variation in temperature, which can occur via thermal dilation, which influence the Λ parameter, and via thermo-optic effect, which influence the n_{eff} parameter. The first term of equation 2.7 shows the effect of temperature in the reflected Bragg wavelength and the second one denotes the effect of the mechanical strain. So, if only change in temperature is considered ($\Delta l = 0$), one gets [17]:

$$\Delta\lambda_B = S_T\Delta T = \lambda_B(\alpha_\Lambda + \alpha_{\mathrm{n}}) \qquad (2.8)$$

where S_T is the thermal sensitivity of the FBG.

The α_Λ parameter is the thermal expansion coefficient of the fiber ($\sim 0.55 \times 10^{-6}\,^{\circ}\mathrm{C}^{-1}$ for silica), and α_{n} is the thermo-optic coefficient ($\sim 8.6 \times 10^{-6}\,^{\circ}\mathrm{C}^{-1}$ for germanium doped silica-core fiber). A thermal sensitivity approximately equal to 13 pm/ºC is expected for FBGs working at the spectral region of 1550 nm [13, 17].

When neglecting the thermal disturbances ($\Delta T = 0$), the effect of mechanical disturbances in the Bragg wavelength is described by equation 2.9 [17]:

$$\Delta\lambda_B = S_{\Delta l}\varepsilon_z = \lambda_B(1 - p_e)\varepsilon_z \qquad (2.9)$$

where $S_{\Delta l}$ is the sensitivity to the strain felt over the longitudinal axis, and ε_z is the relative strain over the longitudinal axis. When the FBG suffers a contraction the ε_z value is negative and when it is expanded this value turns positive.

By integrating the intrinsic interference between the reflected spectra of the FBG and the Fabry-Perot Interferometer (FPI) with respect to the wavelength at each time instant, one gets an optical power variation. This process is called edge filtering, where the FPI acts an optical power discriminator.

D. Modulation techniques

For the proposed AOM system, several modulation techniques can be tested as candidates for a successful transmission of the encoded data that comes from the IoT devices, namely OOK, Amplitude-Shift Keying (ASK) and Frequency-Shift Keying (FSK). Phase related modulations were not considered since the existent system lacks the phase stability required to perform carrier-phase estimation in order to properly modulate the data [20].

The actual tested modulation techniques were the OOK and the FSK. In the context of this system, the OOK modulation technique is used to modulate the optical subcarrier with respect to the frequency, whereas the FSK method is used to modulate an electrical subcarrier with respect to its frequency, which therefore modulates the optical subcarrier in the

frequency domain.

E. On-Off Keying Modulation

The transmission of a binary sequence can be done with use of on-off signals, i.e., when the transmitted bit is 1, the transmitted signal waveform is $s_1(t) = s(t)$, and when the transmitted bit is 0, the signal waveform becomes $s_0(t) = -s(t)$, where $s(t) = A, 0 \leq t \leq T_b$.

These types of signals are known as antipodal signals, since one signal waveform is the negative of the other. Thus, the received signal waveform, after going through a noisy channel, may be represented as:

$$r(t) = \pm s(t) + n(t), \qquad 0 \leq t \leq T_b \tag{2.10}$$

where $n(t)$ represents the additive white Gaussian noise. The optimum receiver consists of a correlator whose output is sampled at $t = T_b$, and followed by a detector that compares the sampled output with a certain threshold valued as α.

For signal waveforms with equal probabilities, the optimum detector compares r with a threshold $\alpha = 0$. If $r > 0$ the detector decides that $s(t)$ was transmitted, whereas when $r < 0$, the decision is made that $-s(t)$ was transmitted [20].

F.Frequency-Shift Keying

With M-ary FSK, it is possible to transmit $k = \log_2 M$ bits per symbol with M signal waveforms which can be expressed in equation 2.11:

$$\hat{u}_m(t) = \sqrt{\frac{2E_s}{T}}\cos(2\pi(f_c + m\Delta f)t) \tag{2.11}$$

for $m = 0, 1, \ldots, M-1$ and $0 \leq t \leq T$, where $E_s = kE_b$ is the energy per symbol (being E_b the signal energy per bit), $T = kT_b$ is the symbol interval (with T_b corresponding to the duration of the bit interval), Δf is the frequency separation and f_c is the carrier frequency [20].

In real life conditions, the received signal is different from the transmitted one, i.e., when the modulated signal goes through a transmission channel, it gets delayed and it is affected by noise, therefore $r_m(t)$ is expressed by:

$$r_m(t) = \sqrt{\frac{2E_s}{T}}\cos(2\pi(f_c + m\Delta f)t + \emptyset(t)) + n(t) \tag{2.12}$$

where, $\emptyset(t)$ represents the phase shift of the mth signal and $n(t)$ is the additive bandpass noise.

When the signals $\{r_{mc}, r_{ms}\}_{m=0}^{M-1}$ have the same probability, the signal envelopes can be computed by the square law detector ${r_m}^2$:

$$r_m^2 = r_{mc}^2 + r_{ms}^2 \tag{2.13}$$

which will then select the signal corresponding to the largest $\{r_m^2\}$ value. Figure 4 depicts the schematic of the discussed process of detection and demodulation for an M-ary FSK received signal, where the basis functions of the correlators feature the known phase shift for each symbol when equalization is not used. This was the approach used in the simulations described in section 5.

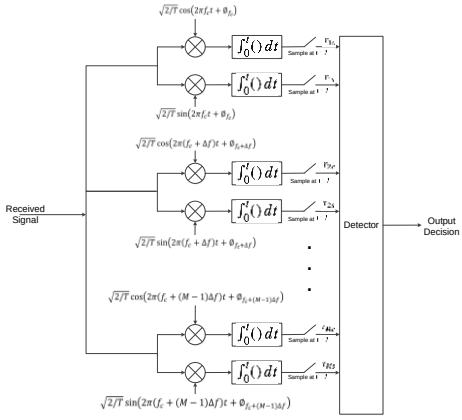

Fig.4. Schematic of the M-ary FSK detection and demodulation process (adapted from [20]).

G.Probability of error for M-ary orthogonal signals

For M-ary orthogonal signals, the probability of error, assuming the symmetry of the signal space and equal probabilities for all M symbols, can be simplified so that only two parameters affect the overall probability, namely M, which is the number of symbols, and E/N_0, which is the signal-to-noise ratio.

$$P_e = \frac{1}{\sqrt{2\pi}}\int_{-\infty}^{\infty}\{1 - [1 - Q(y)]^{M-1}\}e^{-(y-\sqrt{2E/N_0})^2/2}dy \tag{2.14}$$

with $Q(y) = 1/2erfc(y/\sqrt{2})$, M representing the total of symbols for a certain M-ary FSK modulation schemes, E being the symbol energy and $N_0 = \sigma^2/2$, with σ^2 being the noise variance [20].

H.Estimation of the BER from the EVM

Error Vector Magnitude (EVM) is proven to be an appropriate metric for optical channels limited by AWGN. It can be described as the effective distance of the received complex symbol from its ideal position in the constellation diagram. In mathematical terms, a received signal vector E_r deviates from an ideal transmitted vector E_t by an error vector E_{err}.

$${EVM_a}^2 = \frac{M}{I}\frac{\sum_{i=1}^{I}|E_{r,i} - E_{t,i}|^2}{\sum_{i=1}^{M}|E_{t,i}|^2} \tag{2.15}$$

This last parameter is used for the estimation of the BER, whose approximate mathematical expression is shown in equation 2.15, with L being defined as the number of signal levels in each dimension of the constellation, which, in the case of the M-ary FSK modulation, is equal to the number of the M symbols. I is the number of randomly transmitted data [22].

$$BER \approx \frac{(1 - L^{-1})}{\log_2 L}erfc\left[\sqrt{\frac{3\log_2 L}{(L^2 - 1){EVM_a}^2\log_2 M}}\right] \tag{2.16}$$

III. AOM FOR THE IOT

A detailed schematic of the IoToF concept can be seen in figure 5, featuring the five main blocks or stages: the receiver stage, the demodulation stage, the IoT devices, the codification-modulation stage and the AOMs. The multiplexing capability of the FBGs and the inherent low optical fiber attenuation, provides an advantage in a sense that it is possible to distribute several AOMs along the same optical

fiber, with each AOM having its own Bragg wavelength associated with (λ_1, λ_2, …, λ_n). The BBS feeds the AOMs, since the FBGs included in these modulators are completely passive elements, which are mechanically driven by acoustic signals containing the IoT information. Then, an optical circulator redirects the reflected spectra of the FBGs to the several FPIs, located at the receiver stage, which act as linear edge filters.

This allows for the straightforward translation from the spectral shifts from the several existent FBGs, into optical power variations, which are then converted into the electrical domain by the photodetectors, which are also located at the same receiver stage.

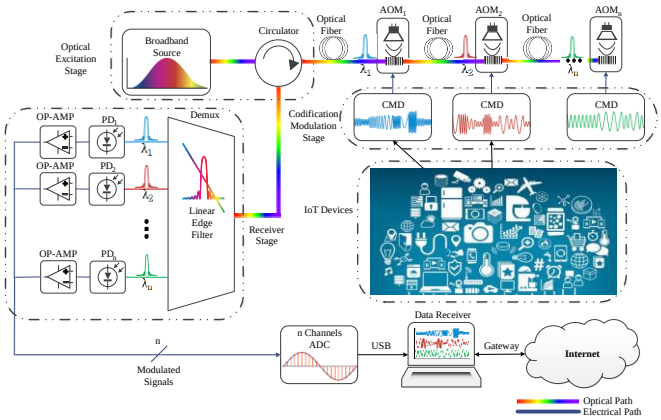

Fig.5. Schematic of the IoT2oF approach.

The electrical signals are amplified by the operational amplifiers (OP-AMPs) in transimpedance configuration and posteriorly acquired by an ADC module. The data receiver is able to process the received signals and demodulate them, which makes possible the sharing of this information with the Internet. However, for this whole process to occur, it is necessary the use of Codification-Modulation Devices (CMDs) which are responsible for the digital modulation and generation of the electrical signals that excite the AOMs, since the AOMs are not able to read the information coming from the IoT devices directly.

Also, the previous schematic can be translated in terms of a PHY functional sub-layers scheme, as depicted in figure 6, with the CMD stage corresponding to the Information-to-Electrical (I/E) phase, the Electrical-to-Acoustic (E/A) phase conversion being the induced mechanical vibrations on the FBG from the speaker, followed by an Acoustic-to-Optical (A/O) conversion, in order for the optical channel to transmit the modulated information through long distances to finally reach the optical receiver, where the received signal undergoes an O/E conversion, done by the photodetectors. Finally, there is the Electrical-to-Digital (E/D) conversion performed by the ADC and the Digital-to-Information (D/I) phase, which contains the demodulation and decision processes.

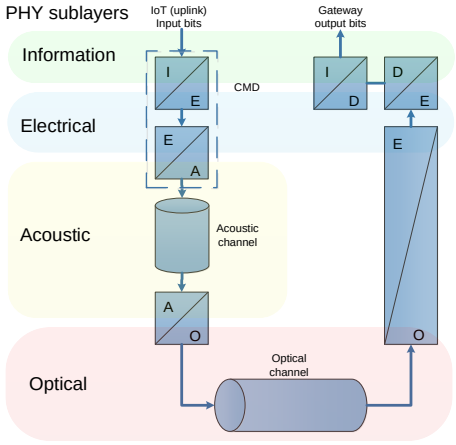

Figure 6: Flowchart of the PHY sublayers communication.

A. Simulator implementation

Figure 7 depicts the block diagram of the implemented simulator that was done with MATLAB. Its working principle can be explained in different phases, with each one having its own functional block:

Input Electrical Signal – The signal that is injected in the system, i.e., the OOK modulated signal or the M-ary FSK modulated signal that contains the information from the first PHY sublayer, depicted in figure 5, in which is applied Gray codification (CMD stage). This type of codification was used in order to reduce the impact of symbol error rate over bit error statistics. The electrical signals applied are converted into acoustic signals because of the transducer of the speaker.

Max. WL shift – Contains the maximum wavelength shift induced in the FBG, which in this case is around 80 pm. This value will be explained in section 4.

System Response Filter – Contains the transfer function of the AOM system, with a bandwidth of 1 kHz and a similar shape to the one from figure 9 (a). Initially there is an imposed delay of around 57 ms in the received signal, which is due to the fact that a Finite Impulse Response (FIR) digital filter was implemented, with order equal to 5000, using the Least-Squares approach, for a sampling rate of 44 kHz, so that a considerably large number of samples per symbol could be acquired. This type of filter has a linear phase response which in turn preserves the waveshape of the input signal, to the extent that is possible, since some frequencies will be changed in amplitude by the action of the filter. The system's phase response was applied to the output signal of the System Response Filter block, using the Fast Fourier Transform (FFT) [23].

Volt to WL – The amplitude of the electrical signal causes the excursion movement of the speaker's diaphragm which will extend or contract the FBG, which in turn causes the Bragg wavelength to change in each time instant. In other words, it is here where the A/O conversion takes place.

WL to FBG – Here the Bragg wavelength obtained in the previous block is substituted in equation 2.6, with the other parameters being $n_{eff} = 1.458$, $L = 10\,mm$ and $\delta n_{eff} = 10^{-4}$. This block calculates the power spectral density spectrum reflected by the FBG for each time instant.

Attenuator – The attenuations in the optical channel from both the optical circulator and the VOA are applied.

FPI – Contains the transfer function depicted in the upcoming figure 4.9 (III). For each time instant, this transfer function will apply an optical power variation to the FBG's reflected spectrum throughout time.

Spectral Density to Power – In this block, the integral of the

interference between the reflected FBG and FPI spectra, with respect to the wavelength, is applied, i.e., the resulting power signal of the interference between the FBG and the FPI spectra is computed.

AWGN Channel – This block serves as way to introduce noise originated from all the optical elements connected in the montage of the system, thus allowing for a study of its performance.

Gain – Contains the responsivity of the photodetector, the gain from the OP-AMP and the resistance value of the ADC. These are responsible for the O/E conversion.

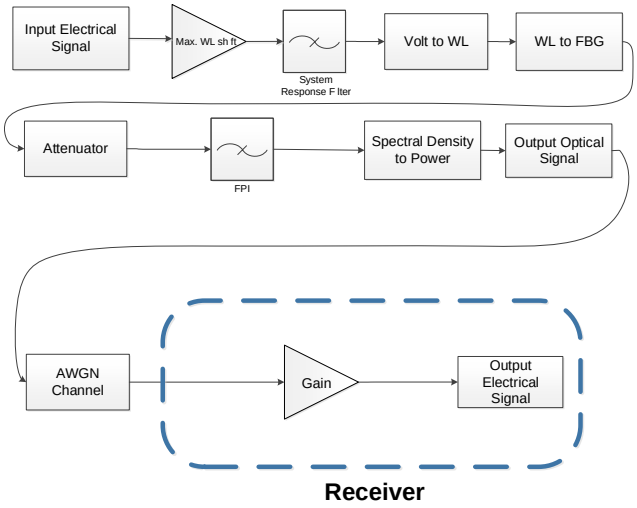

Fig. 7. Block diagram of the implemented simulator.

The signal received in the Output Electrical Signal block, which can be an OOK or M-ary FSK modulated signal with or without equalization, is demodulated, i.e., the E/D conversion happens. Finally, the retrieved digital signal is converted into its corresponding Gray code.

II. System Implementation

A. FBG manufacture

Given the other acousto-optic modulation systems, in this study a low-cost AOM system based on the usage of an FBG and a commercial speaker with a membrane diameter of 48 mm is proposed. A photosensitive SMF (ThorLabs GF1B) was used to record the FBG with the phase mask technique by using an excimer laser emitting at 248 nm in an FBG inducing system built at *Instituto de Telecomunicações – Pólo de Aveiro* (IT).

The operation principle of the proposed AOM is based on the longitudinal movement of the speaker diaphragm (excursion), as depicted in figure 8, which imposes a contraction ($\varepsilon < \varepsilon_0$) and an expansion ($\varepsilon > \varepsilon_0$) in the FBG when the speaker is exposed to a certain applied electrical signal.

When launching an optical signal from a BBS in the fiber, a blueshift or redshift is observed in the FBG reflected spectrum. The Bragg wavelength is thus changed as a function of the external electrical signal that is fed to the speaker.

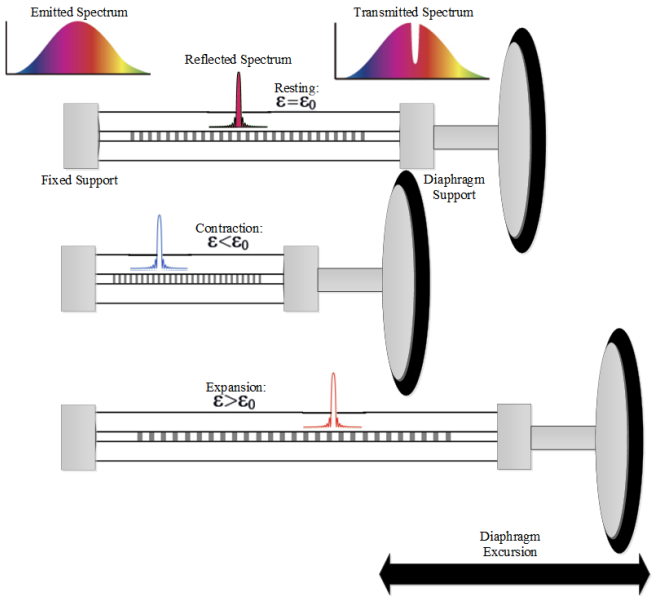

Fig. 8. Schematic of the FBG operation principle.

B. System characterization

For the characterization of both frequency and temporal responses of the proposed system, two analyses were performed. The system response was analyzed by using a $A\sin(\omega t)$ signal generated by the AWG, where $\omega = 2\pi f_c$. The amplitude (A) of the signal was maintained constant (± 1 V) as well as the volume in the speaker. Then, the frequency (f_c) was swept from 10 Hz to 1000 Hz in steps of 10 Hz, with each step lasting a total of 2 seconds, approximately. After obtaining the information regarding the amplitude and phase delay between the reference and the modulated signal, it is possible to determine the transfer function of the system and it is depicted in figure 9.

Figure 9 (a) shows the amplitude transfer function of the system, in which the maximum optical amplitude variation is set between 550 Hz and 650 Hz, where the resonance frequency is evidenced around 570 Hz. It can also be observed that for extreme frequencies, especially for values lower than 50 Hz and higher than 900 Hz, the amplitude is attenuated in more than, approximately, 45 dB, therefore, the effective bandwidth of this solution is around 800 Hz.

(a)

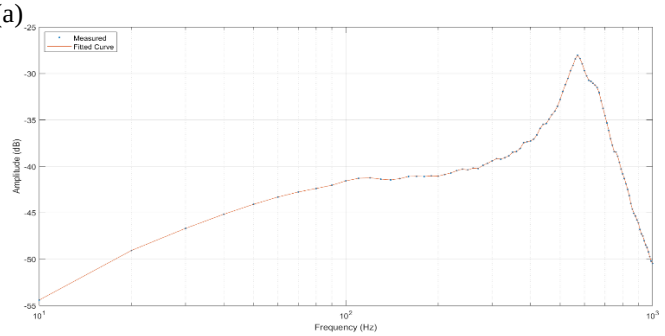

(b)

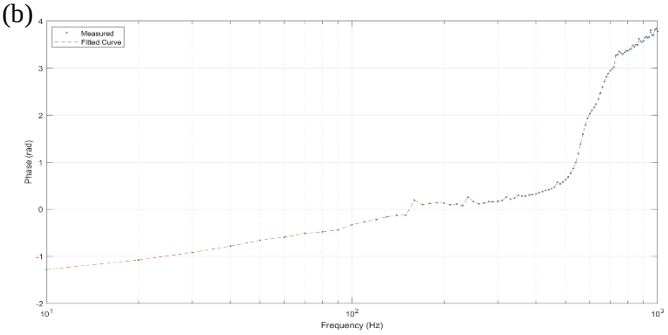

Fig. 9. Amplitude response of the AOM system.

Figure 9 (b) depicts the phase response of the optical-acoustic modulation system, again with the points representing the measured phase delays and line being the estimated phase delays for the in-between frequencies. The minimum phase delay is achieved at around 200 Hz, with an observed linear phase increment from this same frequency up to 500 Hz. Finally, the delay is drastically increased for frequencies higher than 500 Hz, i.e., near the resonance frequency.

Figure 10 depicts the resulting electrical amplitude of the output signal when the input is a sinusoidal of a certain frequency and unitary amplitude. Using the mentioned spectrometer, the Bragg wavelength shift (red solid line) is obtained for every obtained electrical signal (dashed blue line), when the input voltage signal has a frequency that ranges from 10 Hz to around 300 Hz.

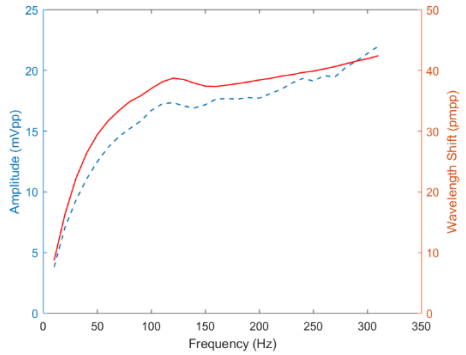

Fig. 10. Wavelength shift versus output amplitude.

By subtracting the obtained wavelengths for each frequency values from the pre-stressed FBG Bragg wavelength ($\lambda_B = 1547.5$ nm) and multiplying them by a factor of 2, the resultant shifts from the lowest to the highest Bragg wavelength are obtained.

From figure 10, one can already deduce, assuming a linear relation between both curves, a relation of around 2 pmpp/mVpp, i.e., there is linear relation between wavelength displacement and the amplitude of the electrical signal received. Knowing that the maximum output voltage, for this implementation, is around 80 mVpp, a maximum wavelength shift of 160 pmpp is obtained, i.e., 80 pm from the central Bragg wavelength to the maximum displacement.

Another characteristic of the system that was analyzed was the pulse response, in which it is possible to observe that for pulse periods lower than 2.5 ms, approximately, there is an increase in the underdamped response, thus the resonance frequency is predominant in the underdamped temporal response.

IV. Simulation Results

Mainly two modulation approaches will be used in the simulations. The first one is the direct FSK modulation, in which the optical carrier is modulated directly, i.e., when the amplitude of the signal is highest, so is the wavelength displacement in the fiber. The second one is the most enticing one, which is to have an FSK subcarrier to modulate the optical one, which will allow for the imprinting of mechanical displacement into frequency modulation. This last was proven to be the most effective one in the experimental work done and it will serve as base for the dimensioning of the implemented simulator's AWGN's noise variance.

In order to perform the simulations, the noise variance was estimated so that, for a transmission line distance of 30 km, a Bit Error Rate (BER) around 0.2% would be measured for the 8-FSK modulation scheme with complex equalization for a total of 10.500 bits. An optical attenuation ranging from 0 to 20 dB, for a 2 dB iteration, was applied, using the bit comparison method. Figure 5.1 depicts the 8, 4 and 2-FSK BER curves for a dimensioned noise variance equal to, approximately, 3.31×10^{-20} W.

V. Performance Assessment for OOK Modulation

With the dimensioned noise variance for the AWGN channel, now it is possible to perform simulations for the assessment of the system's performance. First, the simplest modulation was applied, the OOK one. A binary sequence serves as the input signal, with the -1 V amplitude being encoded with the bit 0 and the +1 V amplitude with the bit 1, so that the rejection in the output signal between the zero level and the one level is as high as possible. A total of 10.500 bits were considered, with the signal duration varying according to the bit rates.

The non-equalized received electrical signal is depicted in figure 11 (a), which was obtained by simply injecting the system with, in this case, the OOK modulated signal. It can be observed that the ISI is quite predominant, since the eye diagram is quite obstructed.

The equalization was done by applying to the modulation carrier the inverse transfer function of the complex transfer function of the system, which is depicted in figure 8. It serves as much more promising modulation for this system, since it reduces the ISI significantly, thus the eye is more opened (figure 10 (b)).

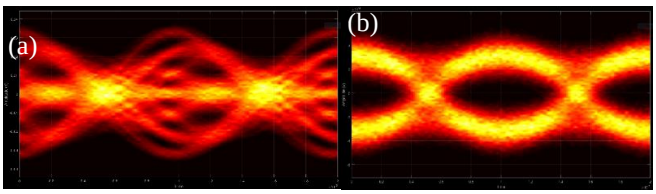

Fig. 11. Eye diagram for the equalized 1000 bps system.

Complex equalization for the OOK modulation scheme can be assessed in relation to its performance in an AWGN channel with the BER estimation. Given the fact that a sequence of randomly transmitted data is generated, i.e., a stochastic process occurs in each simulation that is done, several simulations were done to get a better understanding of the system's performance.

Figure 12 shows the mean BER curves for three simulations done for each bit rate. By applying the previously mentioned process of computing the distances between the detector output values and their mean values for each optical power at the receiver's input.

The dashed black line is the maximum tolerable pre-Forward

Error Correction (FEC) BER, also known as the "FEC-threshold", which, in the context of optical transport networks, is the associated limit BER value for which, when the system performs at a BER lower than this, it is considered as error-free [24].

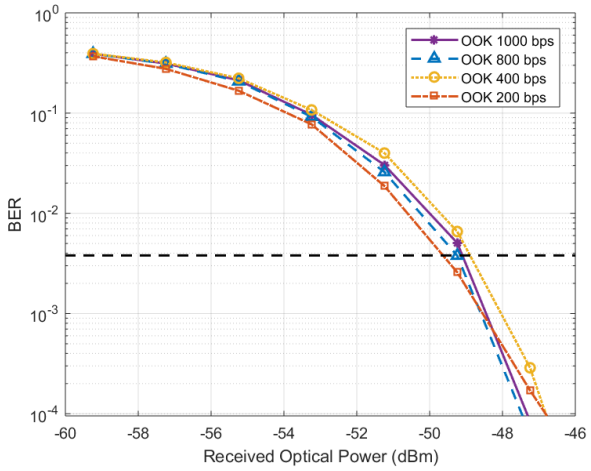

Fig. 12. Eye diagram for the equalized 1000 bps system.

One can observe that, for example, for a power of -49.24 dBm, only the 200 bps equalized OOK modulation can be considered as error-free, with a mean BER value between 0.2% to 0.3%. The other three cases, 800, 1000 and 400 bps, have higher BER values than the pre-FEC BER threshold, with mean BER values of approximately 0.4%, 0.5% and 0.7%, respectively.

Less samples are taken for higher bit rates, with the lowest number of samples being for a bit rate of 1000 bps, whereas in the case of 200 bps, a total of 220 samples are taken. This might influence the obtained results because of the aliasing effect, since there can be an insufficient number of samples to represent each bit. Thus, for higher bit rates, the results are less reliable.

For optical powers higher than -48 dBm, approximately, all the tested bit rates were proven to be successful in the transmission of information and offer data throughputs that are much higher than the one achieved by the Sigfox protocol.

VI. Performance Assessment for M-ary FSK Modulation

Also, taking the equations for the BER estimative from the EVM into account, a comparison between the equalized M-ary FSK modulated schemes can be made. The 8-FSK modulated system has the highest BER for the same received optical power, and the BER for 4-FSK is lower than the previous one but higher than the one from 2-FSK modulated system.

These results were obtained for simulation using a total of 10.500 bits over different durations, varying according to the different bit rates, with the BER curves being the mean values for three simulations, in the case of 2-FSK, another three simulations for 4-FSK, and finally, seven simulations for 8-FSK.

While, for a received optical power of approximately -49.24 dBm, the 2-FSK and 4-FSK systems have a much lower BER than the one from 8-FSK, which is around 4%, i.e., it is higher than the pre-FEC BER value. Thus, one can deduce that for the same received optical power at the receiver's input, the 8-FSK equalized system is much more affected in the transmission link than the others. Next, it will be discussed how the equalized system performs in comparison with the non-equalized one, with BER estimation from EVM method for the same received optical power.

The results for this particular case are unexpected, since the symbol probabilities are equal to one another and this is a case of orthogonal symbols, one can use the probability of error expression, as depicted in equation 2.14, to study this case. It is important to notice that for different energy symbols there is no symmetry of the signal space, but for the stake of simplicity and since this is a case of study that is not in the scope of this study, one can make this assumption.

The fact that the 2-FSK equalized system has an overall higher BER than the non-equalized one, may be due to the fact that the latter has a higher E/N_0 value than the former. Also, for lower noise variance, i.e., for a lower N_0 a result where the equalized system performs in a better way could have been achieved.

For a measured received optical power of -53.24 dBm, one estimates a BER of 0.3% for the equalized system and 0.06% for the non-equalized one, which is lower. But at the same time, both cases can be considered error-free for that same received power. Whereas for lower powers both cases have BER values higher than pre-FEC BER threshold.

In the case of the 4-FSK, the same unexpected conclusion of the 2-FSK modulated system was obtained, although with a much more significant difference.

For a received optical power of -51.24 dBm, the BER for the equalized system is around 2%, whereas for the non-equalized on the BER is around 0.06%, which can be considered error-free and it has significantly better performance overall than the equalized scenario. (a)

Again, the fact that the 4-FSK equalized system has an overall higher BER than the non-equalized one, can be explained with the same analogy used in the 2-FSK scenario. The higher E/N_0 value is due to symbol 3 having the highest energy of all four symbols.

Regarding FSK modulation results, the most promising modulation scheme is the 8-FSK, providing a bit rate of 300 bps, and where a significant difference can be seen when comparing the equalized and non-equalized solutions. A discrepancy between an equalized and a non-equalized 8-FSK system is not unexpected, since the non-equalized solution will induce a significant ISI, especially in the transitions from a high frequency to a low one, as it can be seen in figure 13 (b), being the most evident one the transition from 700 Hz to 100 Hz, in the 0.32 to 0.33 s time interval (marked with a red circle).

In the transition from 700Hz to 100 Hz, the 100 Hz wave has a superimposed harmonic component of the natural frequency. For strong oscillation changes, the underdamped response requires a period of around 12 ms for it to stabilize, which is higher than the minimum period of symbol. This can be considered as ISI and, in case of a transition from a lower to a higher frequency, i.e., neighbor subcarriers, the wave shape is not going to be affected.

When complex equalization is applied, this ISI is removed by applying the inverse transfer function of the system's complex response, thus the wave shape of the signal will not be affected overall. For the example depicted in figure 14 (b), this fact be observed, where there is no longer wave shape distortion in the

800 Hz to 100 Hz transition (marked with a green circle).

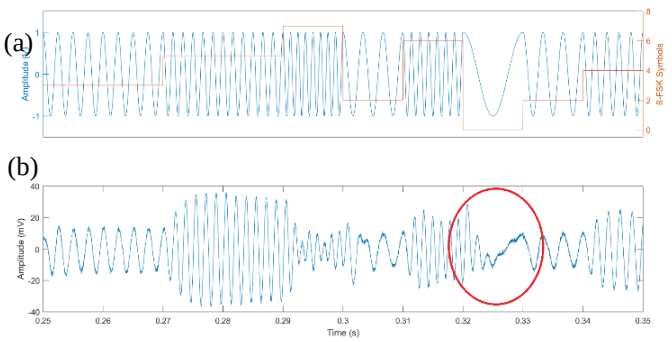

Fig. 13. Non-equalized 8-FSK received signal (b) as a function of the transmitted signal (a).

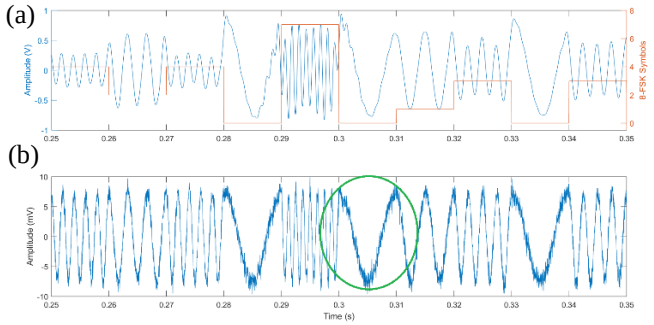

Fig. 14. Equalized 8-FSK received signal (b) as a function of the transmitted signal (a).

Figure 15 depicts the spectra for both non-equalized, on the left side, and equalized, on the right side, 8-FSK systems, where, as expected, the equalized one has the frequencies nearly at the same amplitude, whereas in the case of non-equalization, the 600 Hz, which is near the resonance one, has the biggest amplitude.

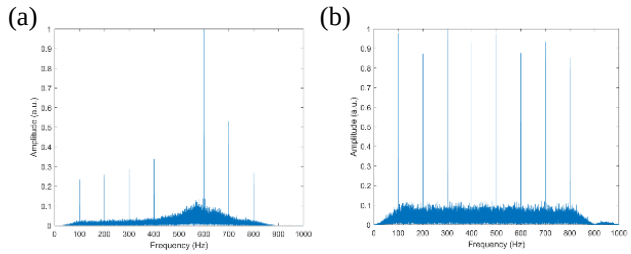

Figure 15: Spectra for both non-equalized (a) and the equalized (b) 8-FSK system.

But confirmation on the advantages of equalization for the 8-FSK solution must obtained with the EVM measure technique. Figure 16 depicts the comparison between the use of equalization and non-equalization, zoomed in for BER values over 0.1%, because the equalized system has much lower BER values for received optical powers between -47 dBm and -39.24 dBm, approximately. The red curve is the mean BER curve for the non-equalized system, for a total of 30 simulations.

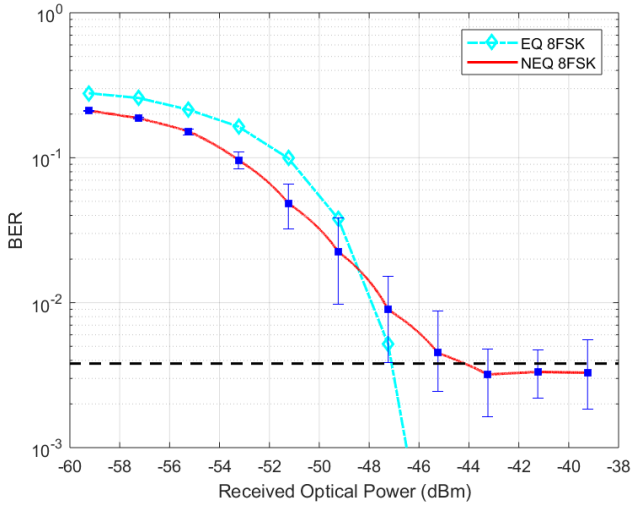

Fig. 16. Comparison between equalized and non-equalized 8-FSK.

Contrary to previous simulations, the measured BER values showed significant deviations from the mean values, so a greater number of simulations needed to be executed, in order to have a better understanding of the overall system performance. Thus, in this case, the error bars were placed in the measured points.

When inspecting the detector output values for a signal power equal to -45.24 dBm, approximately, for the non-equalized situation, symbol 5 has the greatest mean value, which leads to serious consequences for the system's performance.

By thoroughly analyzing all the results regarding M-ary FSK modulation schemes, equalized 8-FSK seemed like the most promising one for the IoToF, with an estimated BER always lower than the pre-FEC threshold until an optical power around -47 dBm, whereas the non-equalized modulation shows much higher BER values for higher optical powers. With this solution, the highest throughput in M-ary FSK modulation was achieved, being also higher than the bit rate of the Sigfox standard and, also, with a higher range than LoRa.

The OOK modulation scheme with complex equalization can also be used for this application, although for an optical power received between -50 dBm and -48 dBm, for bit rates of 400 bps, 800 bps and 1000 bps, this solution does not seem feasible. The best results can be observed when a bit rate of 200 bps is used, which does improve the data throughput that the Sigfox protocol achieves, but has a worse performance than the 4-FSK modulated system, which already is capable of transmitting data at 200 bps. ISI has a significant impact in this system for this scheme, causing the non-equalized OOK solution to be far from ideal.

VII. Laboratorial Results

In collaboration with *Instituto de Telecomunicações – Pólo de Aveiro*, a laboratorial work was done for an arbitrary binary sequence of 3000 bits, with Gray codification, with pre-emphasis equalization for 2, 4 and 8-FSK modulation schemes. The laboratorial setup of the work done can be viewed in figure 17, which is depicted below.

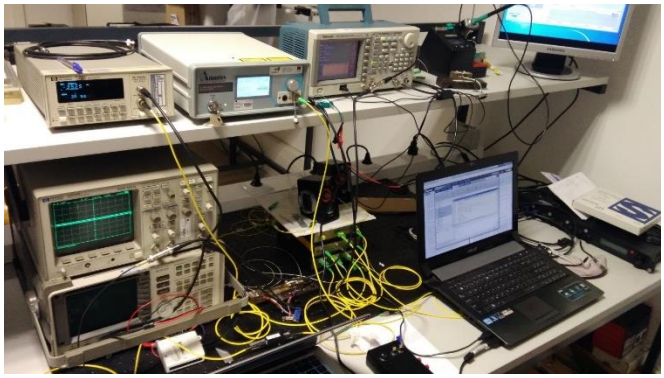

Fig. 17. Photograph of the laboratorial setup.

The system performance was tested as a function of the attenuation applied (0.2 dB/km), with each iteration representing a transmission distance of 5 km. The BER as a function of the transmission distance was analyzed for the several modulation schemes used, with the results being depicted in figure 18.

For the highest bit rate (300 bps), the system is less tolerant to the link attenuation. A comparison was made with a receiver sensitivity of 1%, considered in narrowband wireless systems. For this specific condition, this system offers a maximum transmission distance of around 30 km and an additional distance of 5 km can be added to this for the 4-FSK (200 bps) and 2-FSK (100 bps) [25, 26].

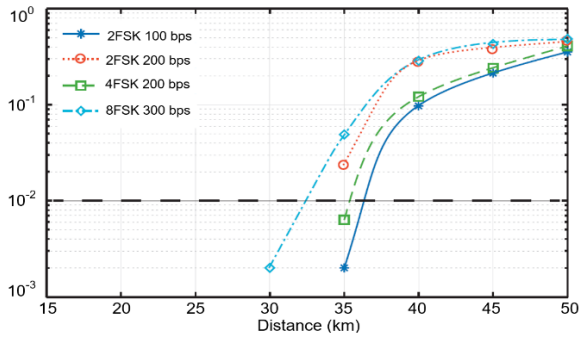

Fig. 18. BER as a function of the transmission distance.

VIII. Conclusions and Future Work

For OOK modulation, the system already reaches a data throughput higher than the Sigfox standard, but has an overall worse performance than the 4-FSK modulated system, in the case of the 200 bps bit rate. Regarding the M-FSK modulation schemes, the optimum solution found in the performance assessment is the equalized 8-FSK system, reaching a data throughput of 300 bps, which is higher than Sigfox, and being error-free until a received optical power of around -47 dBm.

It is important to notice that the acoustic channel can be improved upon by using more elaborate E/A structures to enhance the system's response. The use of a forward error correction and a more powerful BBS would extend the reach of this system beyond what was proven to be possible. Other modulation techniques, such as Quadrature Amplitude Modulation (QAM) and coding strategies might also improve the AOM system's spectral efficiency, thus improving the end-user bit rate. The proposed IoToF technology will need a proper short framing link layer solution over IoToF PHY. Also, another important aspect is the AOM's power consumption, which will consequently influence the IoToF's device autonomy. Distributed Raman amplification can be used to extend the transmission's reach, while its pump power recycling is used for power transmission over the optical fiber, which could be used for feeding IoToF devices [27].

References

1. Kilper, D., et al., *Optical networks come of age*, Optics and Photonics News, Vol. **25**, No. 9, pp. 50-57, 2014.
2. Winzer, P.J., Scaling optical fiber networks: Challenges and solutions. Optics and Photonics News, Vol. 26, No. 3, pp. 28-35, 2015.
3. Madakam, S., R. Ramaswamy, and S. Tripathi, Internet of Things (IoT): A literature review, Journal of Computer and Communications,Vol. 3, No.5, pp. 164, 2015.
4. Ji, P.N. and W. Ting. Internet of things with optical connectivity, networking, and beyond, in 2016 21st OptoElectronics and Communications Conference (OECC) held jointly with 2016 International Conference on Photonics *in Switching (PS)*, Niigata, Jul. 2016.
5. Alkhatib, H., et al., IEEE Computer Society 2022 Report. Recovered by: http://www.computer.org/cms/Computer.org/ComputingNow/2022Report.pdf, 2014.
6. Vetter, P., et al., Energy-efficiency improvements for optical access. IEEE Communications Magazine, Vol. 52, No. 4, pp. 136-144, 2014.
7. Larsen, C.P., A. Gavler, and K. Wang. Comparison of active and passive optical access networks. in Telecommunications Internet and Media Techno Economics (CTTE), 9th Conference, Ghent, Belgium: IEEE, Jun. 2010.
8. Grobe, K., et al., Cost and energy consumption analysis of advanced WDM-PONs. IEEE Communications Magazine, Vol. 49, No. 2, 2011.
9. Senior, J.M. and M.Y. Jamro, Optical fiber communications: principles and practice. Pearson Education. 2009
10. Reiter, G., Wireless connectivity for the Internet of Things. Europe, Vol.433, pp. 868MHz. 2014.
11. Winder, S. and J. Carr, Newnes radio and RF engineering pocket book, Newnes, 2002.
12. Skubic, B., et al., Energy-efficient next-generation optical access networks. IEEE Communications Magazine, Vol. 50, No. 1, 2012.
13. Chen, Q. and P. Lu, Fiber Bragg gratings and their applications as temperature and humidity sensors, Atomic, Molecular and Optical Physics, pp. 235-260, 2008
14. Torres, P., L.C.G. Valente, and M.C.R. Carvalho, Security system for optical communication signals with fiber Bragg gratings, IEEE Transactions on Microwave Theory and Techniques, Vol. 50, No. 1, pp. 13-16, 2002.
15. Zhang, H. and T. Dong. Fiber Bragg Grating Sensor System in the Application of Guarding against Burglary, in 2012 Second International Conference on Intelligent System Design and Engineering Application. 6-7 January, Sanya, Hainan, China, 2012.
16. Erdogan, T., Fiber grating spectra. Journal of Lightwave Technology, Vol. 15, No. 8, pp. 1277-1294, 1997.
17. Antunes, P.F.d.C., Sensores ópticos para monitorização dinâmica de estruturas, in Departamento de Física., Universidade de Aveiro, 2011.
18. Hill, K.O. and G. Meltz, Fiber Bragg grating technology fundamentals and overview. Journal of lightwave technology, Vol. 15, No. 8, pp. 1263-1276, 1997.

19. Othonos, A., et al., Fibre bragg gratings, in Wavelength Filters in Fibre Optics, Springer. pp. 189-269. 2006
20. Proakis, J., M. Salehi, and G. Bauch, Contemporary communication systems using MATLAB. Nelson Education, 2012
21. Hughes, L.W., A simple upper bound on the error probability for orthogonal signals in white noise. IEEE transactions on communications, Vol. 40, No. 4, pp. 670, 1992.
22. Schmogrow, R., et al., Error vector magnitude as a performance measure for advanced modulation formats. IEEE Photonics Technology Letters, Vol. 24, No. 1, pp. 61-63, 2012.
23. Olson, J.D. Finite impulse response filters. in Biomedical digital signal processing, Prentice-Hall, Inc, 1993.
24. Cho, J., C. Xie, and P.J. Winzer, Analysis of soft-decision FEC on non-AWGN channels, Optics Express, Vol. 20, No. 7, pp. 7915-7928, 2012.
25. Texas Instruments, CC1120 High-Performance RF Transceiver for Narrowband Systems. Datasheet Available Online at: http://www.ti.com/lit/ds/symlink/cc1120.pdf (Accessed on June 23 2012), 2015.
26. Hayashi, G., et al. A 10.8 mA Single Chip Transceiver for 430MHz Narrowband Systems in 0.15/spl mu/m CMOS. in Solid-State Circuits Conference, 2006. Digest of Technical Papers. IEEE International. 6-9 February, 2006 IEEE.
27. André, P., et al., Raman amplified access networks with pump signal recycling for electrical power conversion. Microwave and Optical Technology Letters, Vol. 54, No. 1, pp. 116-119, 2012.